

TEC-0126

Automated Cartographic Feature Attribution Using Panchromatic and Hyperspectral Imagery

David M. McKeown, Jr., et al.

Carnegie Mellon University
Computer Science Department
Digital Mapping Laboratory
5000 Forbes Avenue
Pittsburgh, PA 15213-3891

November 1999

19991115 054

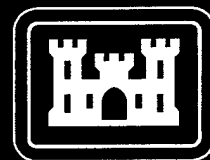
Approved for public release; distribution is unlimited.

Prepared for:

Defense Advanced Research Projects Agency
3701 North Fairfax Drive
Arlington, VA 22203-1714

Monitored by:

U.S. Army Corps of Engineers
Topographic Engineering Center
7701 Telegraph Road
Alexandria, Virginia 22315-3864

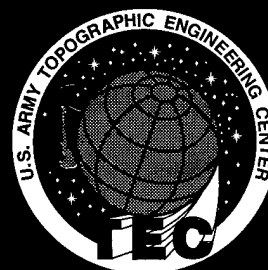


US Army Corps
of Engineers
Topographic
Engineering Center

T

E

C



**Destroy this report when no longer needed.
Do not return it to the originator.**

The findings in this report are not to be construed as an official Department of the Army position unless so designated by other authorized documents.

The citation in this report of trade names of commercially available products does not constitute official endorsement or approval of the use of such products.

| REPORT DOCUMENTATION PAGE | | | <i>Form Approved</i> OMB No. 0704-0188 | |
|--|------------------------------------|---|--|--|
| Public reporting burden for this collection of information is estimated to average 1 hour per response, including the time for reviewing instructions, searching existing data sources, gathering and maintaining the data needed, and completing and reviewing this collection of information. Send comments regarding this burden estimate or any other aspect of this collection of information, including suggestions for reducing this burden to Department of Defense, Washington Headquarters Services, Directorate for Information Operations and Reports (0704-0188), 1215 Jefferson Davis Highway, Suite 1204, Arlington, VA 22202-4302. Respondents should be aware that notwithstanding any other provision of law, no person shall be subject to any penalty for failing to comply with a collection of information if it does not display a currently valid OMB control number. PLEASE DO NOT RETURN YOUR FORM TO THE ABOVE ADDRESS. | | | | |
| 1. REPORT DATE (DD-MM-YYYY) November 1999 | | 2. REPORT TYPE First Annual - Technical | | 3. DATES COVERED (From - To) April 1997 - March 1998 |
| 4. TITLE AND SUBTITLE Automated Cartographic Feature Attribution Using Panchromatic and Hyperspectral Imagery | | | 5a. CONTRACT NUMBER DACA76-97-K0004 | |
| | | | 5b. GRANT NUMBER | |
| | | | 5c. PROGRAM ELEMENT NUMBER | |
| 6. AUTHOR(S) David M. McKeown, Jr., J. Chris McGlone, Stephen J. Ford, Steven D. Cochran, Jefferey A. Shufelt, Wilson A. Harvey, Daniel A. Yocum | | | 5d. PROJECT NUMBER | |
| | | | 5e. TASK NUMBER | |
| | | | 5f. WORK UNIT NUMBER | |
| 7. PERFORMING ORGANIZATION NAME(S) AND ADDRESS(ES) Carnegie Mellon University Computer Science Department Digital Mapping Laboratory 5000 Forbes Avenue Pittsburgh, PA 15213-3891 | | | 8. PERFORMING ORGANIZATION REPORT NUMBER | |
| 9. SPONSORING / MONITORING AGENCY NAME(S) AND ADDRESS(ES) Defense Advanced Research Projects Agency 3701 North Fairfax Drive Arlington, VA 22203-1714 | | | 10. SPONSOR/MONITOR'S ACRONYM(S) | |
| | | | 11. SPONSOR/MONITOR'S REPORT NUMBER(S) TEC-0126 | |
| 12. DISTRIBUTION / AVAILABILITY STATEMENT Approved for public release; distribution is unlimited. | | | | |
| 13. SUPPLEMENTARY NOTES | | | | |
| 14. ABSTRACT The first part of this report describes experiments in the block adjustment of linear pushbroom sensor imagery incorporating object-space straight-line constraints. Both polynomial and interpolative platform models were tested; the polynomial model generally performed better than the interpolative model without lines, but not as well as the interpolative model with straight line constraints. The greater flexibility of the interpolative model makes it better able to describe complex platform motion and to use the geometric strength given by the straight-line constraints, at the expense of increased sensitivity to uneven point distributions or bad points. The second part described current quantitative classification results for man-made and natural materials using 14 surface material classes over selected test areas with Fort Hood. Radiometric effects due to changing solar illumination and atmospheric conditions during the acquisition issues also are discussed. | | | | |
| 15. SUBJECT TERMS block adjustment, linear pushbroom, geometric constraints, HYDICE/hyperspectral imagery, surface material classification, cartographic feature extraction | | | | |
| 16. SECURITY CLASSIFICATION OF: UNCLASSIFIED | | | 17. LIMITATION OF ABSTRACT UNLIMITED | 18. NUMBER OF PAGES 22 |
| a. REPORT UNCLASSIFIED | b. ABSTRACT UNCLASSIFIED | c. THIS PAGE UNCLASSIFIED | | |
| | | | 19b. TELEPHONE NUMBER (include area code) (703) 428-6022 | |

Table of Contents

| TITLE | PAGE |
|---|-----------|
| List of Figures | iv |
| List of Tables | iv |
| Preface | v |
| 1. Introduction | 1 |
| 1.1 Background for CMU APGD Research Project | 1 |
| 1.2 Geometric and radiometric issues | 2 |
| 1.3 HYDICE Data acquisition | 2 |
| 2. Block Adjustment of Linear Pushbroom Imagery with Geometric Constraints | 2 |
| 2.1 Related work | 3 |
| 2.2 The HYDICE sensor geometry | 4 |
| 2.3 Mathematical model | 4 |
| 2.3.1 Linear pushbroom sensor model | 4 |
| 2.3.2 Platform model. | 4 |
| 2.3.3 Block adjustment procedure | 5 |
| 2.3.4 Straight-line geometric constraints | 5 |
| 2.4 Experimental plan | 6 |
| 2.4.1 Source imagery | 6 |
| 2.4.2 Experimental data set | 6 |
| 2.4.3 Evaluation procedure | 6 |
| 2.5 Block Adjustment | 8 |
| 3. Automated Analysis of HYDICE imagery | 11 |
| 4. Conclusions | 14 |
| References | 16 |

List of Figures

| | | |
|---|---|----|
| 1 | HYDICE test images, with tie points, check points, and constrained lines. | 7 |
| 2 | Point test cases, check points, and image coverages. | 8 |
| 3 | Median absolute XY check-point error, meters. | 9 |
| 4 | Check point errors for interpolative model with line constraints. | 10 |
| 5 | Simulated Daedalus ATM near infrared imagery (Band 7) of classification test areas. | 11 |
| 6 | Test area subsection surface material classification. | 12 |

List of Tables

| | | |
|---|---|----|
| 1 | Point test cases. | 8 |
| 2 | Check-point error (meters) for HYDICE images. | 9 |
| 3 | Check-point error (meters) on each HYDICE image, using interpolative model. | 10 |
| 4 | Daedalus ATM spectral bandpasses. | 12 |
| 5 | Fine-to-coarse class grouping. | 13 |
| 6 | RADT9 top 5 confusion pairs. | 13 |
| 7 | CHAFFEE top 5 confusion pairs. | 13 |
| 8 | RADT9 coarse classification error matrix. | 14 |
| 9 | CHAFFEE coarse classification error matrix. | 14 |

Preface

This research was sponsored by the Defense Advanced Research projects Agency (DARPA) and monitored by the U.S. Army Topographic Engineering Center (TEC), under Contract DACA76-97-K-0004, titled, "Automated Cartographic Feature Attribution Using Panchromatic and Hyperspectral Imagery." The DARPA point of contact is Mr. George Lukes, and the TEC Contracting Officer's Representative is Ms. Laretta Williams.

Automated Cartographic Feature Attribution Using Panchromatic and Hyperspectral Imagery

DARPA/APGD Yearly Report 1997–1998

1. Introduction

This report summarizes the primary accomplishments made during the first year of the Defense Advanced Research Projects Agency (DARPA) Automated Population of Geographic Databases (APGD) program. Prior to this contract, late in 1995, we organized a hyperspectral data acquisition using the Naval Research Laboratory's (NRL) Hyperspectral Digital Imagery Collection Experiment (HYDICE) sensor system over Fort Hood, TX. This acquisition resulted in hyperspectral data with a nominal 2-meter ground sample distance collected with 210 spectral samples per pixel. This data formed the basis of our program of research under APGD.

Section 2. describes experiments in the block adjustment of linear pushbroom sensor imagery incorporating object-space straight line constraints. Both polynomial and interpolative platform models were tested; the polynomial model generally performed better than the interpolative model without lines, but not as well as the interpolative model with straight line constraints. The greater flexibility of the interpolative model makes it better able to describe complex platform motion and to use the geometric strength given by the straight line constraints, at the expense of increased sensitivity to uneven point distributions or bad points [McGlone, 1998].

Section 3. describes current quantitative classification results for man-made and natural materials using 14 surface material classes over selected test areas within Fort Hood. We discuss the issues encountered in radiometric effects due to changing solar illumination and atmospheric conditions during the acquisition [Ford *et al.*, 1998].

1.1 Background for CMU APGD Research Project

A major focus of this research during the last 5 years has been the use of multispectral imagery to generate surface material maps. Surface material information is of interest to us both for cartographic feature extraction (CFE), to generate feature hypotheses or to refine features generated by other CFE systems, and for visual simulation, to select realistic visual textures.

Some of our previous research in fusion has involved the combination of surface material information with high-resolution stereo elevation data to produce more refined surface material maps and to aid in distinguishing man-made structures within the scene [Ford and McKeown, 1992a], [Ford and McKeown, 1992b]. We are currently studying the combination of surface material maps with automatically extracted buildings and roads for editing and verification.

One important limitation in this work has been the limited spatial resolution (8–20 meters) of available multispectral imagery. Since we require the precise delineation of object boundaries and the attribution of surface materials for small regions, such as those found within urban areas, we typically work with panchromatic imagery with ground sample distances (GSD) of 0.3 to 1.0 meters. Combining classification results from multispectral imagery with much coarser spatial resolution imposes limitations on the utility of the fusion.

In order to obtain data with higher spatial and spectral resolution we organized a hyperspectral data acquisition using the NRL HYDICE sensor. This acquisition, in October 1995, resulted in hyperspectral data with a nominal 2-meter GSD collected with 210 spectral samples per pixel. The acquisition covered 56 km² over Fort Hood, TX, a site that has been used extensively in the DARPA Image Understanding community to support experiments in semi-automated and automated CFE.

1.2 Geometric and radiometric issues

Two major problems, radiometry and geopositioning, must be addressed in order to effectively use the HYDICE imagery in conjunction with other types of imagery (panchromatic, radar, lidar) used for cartographic feature extraction.

The radiometric problems arise from the effects of changing atmospheric conditions and solar illumination on the ground-reflected spectral radiance collected by the hyperspectral sensor. In order to compare surface material properties between flightlines and to use spectral field measurements of surface materials for spectral analysis, atmospheric corrections are applied to convert HYDICE radiance imagery to apparent reflectance.

Geometric issues are due to the dynamic nature of the image acquisition process and to the weak geometric configuration of the sensor, as discussed below, in "Registration of HYDICE Imagery." For large-scale mapping or more standard remote sensing applications, accurate positioning has been less important; however, to meet our goals of fusing surface material regions with features derived from our road and building extraction systems for high-resolution site modeling, extremely accurate absolute geopositioning and relative registration between images must be established.

1.3 HYDICE Data acquisition

The collection of data at Fort Hood included both airborne imagery and ground truth measurements. The image acquisition included hyperspectral imagery collected by the HYDICE sensor system and natural color film shot by a KS-87 frame reconnaissance camera. The spectral range of the HYDICE sensor extends from the visible to the short wave infrared (400–2500 nm) regions, divided into 210 channels with nominal 10 nm bandwidths.

Nine HYDICE flightlines, each 640 meters wide (cross-track) and 12.6 km long (along-track), were flown over Fort Hood's motor pool, barracks, and main complex areas from an altitude of approximately 4,000 meters above ground level. After each flightline, the HYDICE sensor was flown over and imaged a six-step (2, 4, 8, 16, 32 and 64 percent) gray-scale panel, providing in-scene radiometric calibration measurements for each flightline. Prior to the start of the HYDICE flight collection, several ground spectral measurements were made for each gray level panel in an attempt to characterize its mean spectral reflectance curve. A more detailed description of the HYDICE sensor system, Fort Hood image acquisition and ground truthing activities, can be found in [Ford *et al.*, 1997a].

2. Block Adjustment of Linear Pushbroom Imagery with Geometric Constraints

Linear pushbroom imaging sensors have become widely used within the last few years as a cost-effective means to obtain aerial digital imagery. Linear arrays are less expensive to fabricate than area arrays and require no moving parts, unlike scanners or panoramic cameras.

The main drawback to the use of linear pushbroom sensors is their weak geometry; each image line is, in effect, an independent one-dimensional image. Resecting an individual line is an indeterminate problem, while using the whole image requires that a model of the platform motion as a function of time be solved. The availability of accurate navigation data, such as differential GPS and high-resolution Inertial Navigation System (INS) sensors, has alleviated this problem somewhat. Another approach has been to use multiple linear arrays, pointing in the nadir and off-nadir directions, to improve the geometry by obtaining a wider cone of rays from the same sensor position and also to allow stereo viewing. Examples of this configuration include the Monocular Electro-Optical Stereo Scanner (MEOSS) and the Modular Optoelectronic Multispectral Stereo (MOMS-02) sensors [Ohloff, 1995].

This annual report describes block adjustment experiments using linear pushbroom and frame imagery. This solution differs somewhat from current practice in that only limited navigation information (nominal GPS positions) was available, due to equipment problems during data acquisition. While these experiments may not appear directly relevant to the state of the art, they are important for several reasons:

- From a practical standpoint, navigation equipment sometimes fails and reflights are not always an option. Alternative methods of positioning can be necessary.
- Navigation information may not provide sufficient absolute positioning accuracy due to the inherent errors of the navigation sensors. As higher-resolution digital imagery becomes available, the positioning requirements will become greater. These requirements may be met by improving navigation sensors or by adding additional information to the solution; the choice is a matter of the economics of the particular system. A related issue is the discrete nature of the positioning information, which is available only at intervals. Sensor behavior between readings must be interpolated, on the assumption that the characteristics of the platform motion do not change. Adding external information between reference points will make this interpolation more valid.
- An increasing amount of work is currently being devoted to the fusion of imagery from different sensors, taken at different times. While each set of imagery may be positioned to some level of absolute accuracy, the accumulated relative error between image sets may make fusion difficult. A simultaneous adjustment of all the imagery, with additional information in the form of tie points and geometric constraints, is necessary in such a case.
- Positioning from navigation data alone is inherently open-loop, in that there is no external verification or redundant determination of the positions. For this reason, most block solutions based on navigation information use a few control points to establish the datum for verification purposes. This level of redundancy is adequate for well-calibrated photogrammetric systems; however, for experimental remote sensing systems such as the HYDICE, which are not designed as mapping systems, the system calibration may not be sufficient for reasonable positioning accuracy. Including external data can provide assurances on the quality of the results and also insights into any calibration deficiencies.

The main topics in these experiments were evaluating the differences between polynomial and interpolative platform models and evaluating the use of geometric information, straight lines in the scene, to improve the block adjustment.

Our interest in HYDICE positioning is driven by two main goals. First, we want to generate high-resolution surface material maps, for densification of land-cover information and for realistic material rendering in visual simulation databases [Ford *et al.*, 1998]. Our second goal is to support work in the fusion of disparate types of image information, in order to improve cartographic feature extraction [Ford and McKeown, 1992b; Ford *et al.*, 1997b]. While some amount of mis-registration can be corrected by local refinement during the fusion process, an inaccurate initial registration greatly increases the amount of down-stream work required and may adversely impact the final quality of the fusion results.

2.1 Related work

Most recent work on the orientation of linear pushbroom sensors has been focused on satellite sensors, especially SPOT [Kratky, 1989] and MOMS-02 [Ohloff, 1995]. This differs from the airborne problem in that the platform motion is smoother and is determined by the orbital parameters.

In airborne work, [Heipke *et al.*, 1996] summarize work on the airborne test data from the MEOSS sensor, which uses three linear arrays, (forward-, nadir-, and backward-looking), to obtain stronger geometry. They use an interpolative platform model with full navigation information and a large number of automatically-generated tie points in a block adjustment of four image strips.

Most work on using geometric constraints for orientation has been done using frame imagery [Mikhail, 1993], applying projective geometry to relate image- and object-space lines. The research described in this annual report is most closely related to [McGlone and Mikhail, 1981; McGlone and Mikhail, 1982; McGlone and Mikhail, 1985], which applied straight-line constraints in the block adjustment of airborne multispectral scanner data, and [Paderes *et al.*, 1984], which used lines in the rectification of SPOT imagery.

2.2 The HYDICE sensor geometry

HYperspectral Digital Imagery Collection Experiment (HYDICE) is an experimental 210-channel hyperspectral imaging system developed by the Naval Research Laboratory. The HYDICE sensor is geometrically a linear pushbroom sensor 320 pixels wide; each pixel has an instantaneous field of view of 0.5 milliradians, giving a total field of view of approximately 9 degrees. Physically, the sensor is an area array, with each row of the array producing one band of the image by imaging the incident energy from a different portion of the spectrum. The spectral range of the HYDICE sensor extends from the visible to the short wave infrared regions (400 to 2500 nm), divided into 210 channels. The channel bandwidths range from 7.6 to 14.9 nm, depending on the channel location in the electromagnetic spectrum.

Ancillary navigation and environmental information is recorded during the acquisition of HYDICE imagery. This includes INS and GPS position and orientation data, flight stabilization platform angles, and instrument engineering measurements. More detailed descriptions of the HYDICE sensor system can be found elsewhere [Kappus *et al.*, 1996].

Unfortunately, equipment failures during flight and some problems in system integration resulted in most of the navigation data being unusable. Turbulent atmospheric conditions, unavoidable due to sensor scheduling constraints, also degraded the geometry of the imagery.

2.3 Mathematical model

The mathematical model has several different parts; the sensor model, which describes the imaging geometry of the linear pushbroom sensor, the platform model, a representation of the aircraft position and orientation with respect to time, and the block adjustment incorporating the geometric (straight line) constraints. This section discusses each aspect of the mathematical model.

2.3.1 Linear pushbroom sensor model

A linear pushbroom sensor can be thought of as a frame sensor with only one line in the x , or flight line, direction. The collinearity equations, modified for use with linear pushbroom imagery, are [McGlone, 1996]:

$$\begin{aligned} \begin{bmatrix} U \\ V \\ W \end{bmatrix} &= M_{3,3} \begin{bmatrix} X_p - X_c \\ Y_p - Y_c \\ Z_p - Z_c \end{bmatrix} \\ 0 &= \frac{U}{W} \\ y - y_0 &= -f \frac{V}{W} \end{aligned} \tag{1}$$

where the x coordinate is 0, y is the image coordinate and y_0 is the principal point along the sensor, f is the focal length, and X_p, Y_p, Z_p are cartesian world coordinates of the point. The position parameters, X_c, Y_c, Z_c , and the angular orientation parameters ω, ϕ, κ , (which determine the orientation matrix $M_{3,3}$) are given by the platform model as functions of time, or equivalently, of line number.

Not all of the six orientation parameters can usually be recovered in a resection solution, due to the linear sensor geometry. The ϕ (pitch) angle is highly correlated with position along the flight line, while the narrow field-of-view and lack of terrain relief means that the ω (roll) angle is correlated with the cross-strip position. Without external information, such as angles or positions from navigation sensors, the ω and ϕ parameters must be held to 0 in the adjustment.

2.3.2 Platform model.

The platform model describes the behavior of the orientation parameters as a function of time or line number. Two different models were studied in this work, the polynomial model and the interpolative model.

Polynomial platform model. In the polynomial platform model, the value of each parameter ($X_c, Y_c, Z_c, \omega, \phi, \kappa$) at a particular line is written as a polynomial function of line number x . The block adjustment solution determines the polynomial coefficients, instead of the parameters themselves.

To model complex platform motions over a long period of time would require high-order polynomials, which could lead to unstable solutions. Instead, the flight line is divided into sections, with each section having its own set of lower-order polynomials (in this case, cubic). Continuity constraints on the orientation parameters at the section boundaries ensure that calculated ground positions are continuous across the boundary.

Interpolative platform model The interpolative model stores the orientation parameters of reference lines at regular intervals, then calculates the parameters of intervening image lines by polynomial interpolation. In this case, two reference lines on either side of the line of interest are used, resulting in a cubic interpolation polynomial [Press *et al.*, 1989].

The interpolative model has become more widely used in recent years since navigation data are usually available to specify the parameters of the reference lines. When no navigation data are available, as is the case with this data set, the parameters of each reference line must be solved in the adjustment. If no control or tie points are within the interpolation range of a particular reference line, the parameters of that line will not be adjusted. A continuity constraint is applied between reference lines to ensure that all lines have consistent parameters.

2.3.3 Block adjustment procedure

The bundle block adjustment is performed using an object-oriented photogrammetry package [McGlone, 1995] that allows the use of images with different geometries and the rigorous incorporation of geometric constraints.

2.3.4 Straight-line geometric constraints

Straight-line constraints effectively provide a tie point in each image line, particularly important in this case where no navigation data are available and the imagery is severely deformed. The straight lines are easy to obtain interactively from the imagery, and do not require field surveying or additional navigational equipment.

The equation of a straight line is written as [Mikhail, 1993]:

$$\alpha(X - X_0) + \beta(Y - Y_0) + \gamma(Z - Z_0) = 0 \quad (2)$$

The line equation has six parameters, 4 of which are independent. The direction of the line is represented by the direction cosines α, β, γ , while the location is fixed by specifying the coordinates of a reference point on the line, X_0, Y_0, Z_0 , and constraining that point to be the point on the line closest to the origin.

Two additional constraint equations are required:

$$\begin{aligned} \alpha^2 + \beta^2 + \gamma^2 &= 1 \\ X_0 \alpha + Y_0 \beta + Z_0 \gamma &= 0 \end{aligned} \quad (3)$$

The first constraint normalizes the direction cosines, while the second constraint equation is necessary to give a unique definition of the reference point.

Saying that the projection of an image point, x_i, y_i , lies on a given line in object space is equivalent to saying that the vector (image ray) from the perspective center, X_c, Y_c, Z_c , through the image point, with direction cosines $\alpha_i, \beta_i, \gamma_i$ is coplanar with the line vector α, β, γ through point X_0, Y_0, Z_0 . This is expressed by the scalar triple product:

$$\begin{vmatrix} X_0 - X_c & Y_0 - Y_c & Z_0 - Z_c \\ \alpha & \beta & \gamma \\ \alpha_i & \beta_i & \gamma_i \end{vmatrix} = 0 \quad (4)$$

An important consideration in the use of constraints is efficiency. This has two aspects; reducing the number of parameters involved, and formulating the equations to allow the most efficient normal equation structure. The straight line constraint is written so that point object space coordinates are not explicitly referenced in the equations, thereby reducing the number of total number of parameters in the solution. This also means that corresponding points do not have to be identified and measured on all images, thereby simplifying the measurement process.

2.4 Experimental plan

2.4.1 Source imagery

Three sets of imagery are available over Ft. Hood and will be used in the final block adjustment of the HYDICE imagery.

- The HYDICE imagery, collected in nine sidelapping flight lines with a ground sample distance (GSD) of 2-meters.
- KS-87 color frame imagery, also collected on the HYDICE flights. The KS-87 is an uncalibrated frame reconnaissance camera with a 6-inch focal length and a 5-inch format. The imagery was scanned at a 1-meter GSD.
- The Research And Development for Image Understanding Systems (RADIUS) Ft. Hood imagery. These are about 40 nadir and oblique images, taken with a frame mapping camera and scanned at a GSD of 0.3-meters for the vertical images. These images have been previously block adjusted using surveyed ground control, and provide the basic geometric strength for the adjustment.

The control points for the adjustment were originally surveyed for the adjustment of the RADIUS images. Tie points are measured between all images.

2.4.2 Experimental data set

For the purposes of this annual report, a small sub-block of the available data is being used. The sub-block includes two sidelapping 1,280-line HYDICE images, four KS-87 images, and four RADIUS vertical images. Tie points between the HYDICE images and the frame images were established by manual measurement, with all tie points being measured on at least two frame images. Straight lines also were measured manually on at least two frame images. The two HYDICE images used are shown in Figure 1. Tie points for the heavy density case (described below) are shown as diamonds while check points are shown as crosses. The straight lines used in the solution also are shown.

Three levels of tie point density were established, as shown in Figure 2 and Table 1.

The same 37 check points shown in Figures 1 and 2(d) were used for each experiment. Check points that appear on both HYDICE images are counted twice, as they are treated independently.

All measured object-space straight lines were horizontal and were constrained to be horizontal.

2.4.3 Evaluation procedure

Evaluation was done by comparing the calculated world X,Y coordinates of the check points against the values using the frame images. No evaluation was done on the Z coordinate, since the HYDICE sensor has a very narrow field-of-view (9 degrees) and elevation recovery is weak. For this reason, the Z coordinates of the check points were held fixed in the solution, and points that appeared on both HYDICE images were evaluated as two separate points. Deviations in the X, Y, and XY coordinates were calculated in a local vertical coordinate system, with X being east and Y north. In this case, X also corresponds to the along-strip direction and Y to the cross-strip direction.

In order to gain a better understanding of the characteristics of the solution, three different statistics were calculated: the median absolute deviation, the root-mean-square (RMS) deviation, and the maximum absolute deviation. Since the RMS statistic is extremely sensitive to large outliers, the median and maximum statistics are used to give a better sense of the distribution.



(a) 4.3.

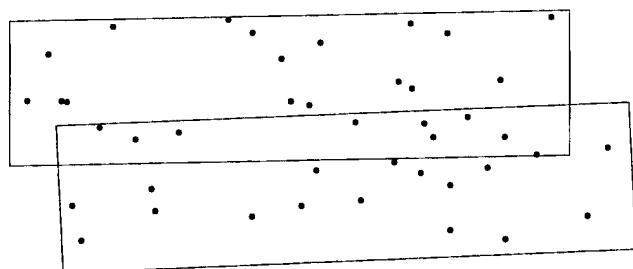


(b) 5.3.

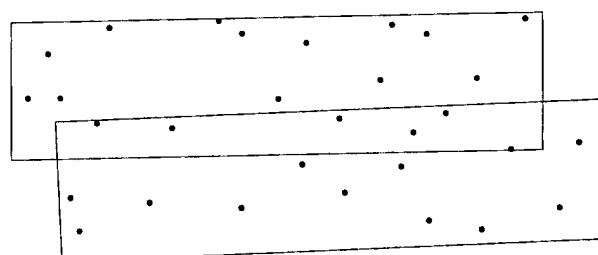
Figure 1: HYDICE test images, with tie points (diamonds), check points (crosses), and constrained lines. North is to the left.

Table 1: Point test cases.

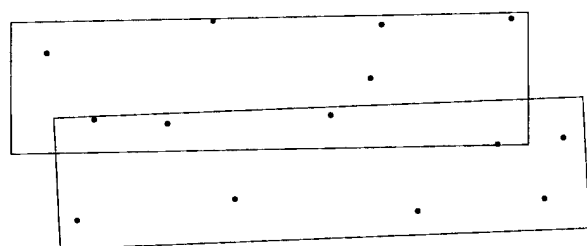
| Case | Figure | Pts on 4_3 | Pts on 5_3 | Pts on both |
|------------|--------|------------|------------|-------------|
| 1 (heavy) | 2(a) | 18 | 17 | 8 |
| 2 (medium) | 2(b) | 14 | 12 | 5 |
| 3 (sparse) | 2(c) | 6 | 6 | 3 |



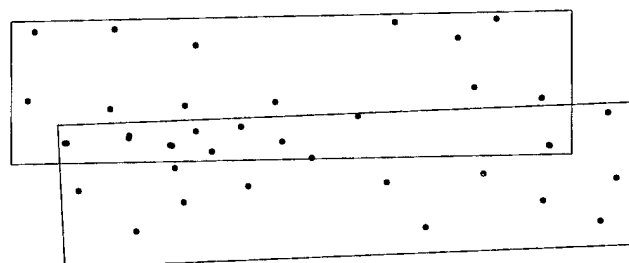
(a) Point case 1 (heavy).



(b) Point case 2 (medium).



(c) Point case 3 (sparse).



(d) Check points.

Figure 2: Point test cases, check points, and image coverages.

2.5 Block Adjustment

The results of the evaluation runs are given in Table 2 and graphically in Figure 3. The interpolative model solution for the sparse point case (3) with no lines and 32-line spacing did not converge, due to weak geometry with the reduced number of points, so no results are given.

We rely mostly on the median statistics in analyzing the results, due to the characteristics of the check-point errors. The test runs show that there are often one or two very large check-point deviations, not representative of the rest of the points. The RMS is greatly affected by these large values, as opposed to the median, which gives a better sense of how most of the points behaved.

Polynomial vs. interpolative platform models. The motion of an airborne platform can be incredibly complex, with its characteristics changing during flight. For instance, compare the differences in deformation between images 4_3 (Figure 1(a)) and 5_3 (Figure 1(b)), from adjacent flight lines; in particular, straight roads and buildings are much more severely deformed in 5_3 than in 4_3. Whether it is derived from navigation data, by a resection solution, or a combination of both, the platform model must meet a set of contradictory requirements. It must have enough degrees of freedom to model the actual motion with high fidelity, while too many degrees of freedom may result in an unstable solution susceptible to bad measurements. Insufficient degrees of freedom will result in aliasing, with unpredictable results between control points.

Table 2: Check-point error (meters) for HYDICE images.

| Model | Pt case | Lines | Ref. line spacing | X | | | Y | | | XY | | |
|--------|---------|-------|-------------------|------------------|------|------|------|------|------|------|------|------|
| | | | | Med | RMS | Max | Med | RMS | Max | Med | RMS | Max |
| Poly | 1 | N | - | 3.1 | 5.3 | 10.6 | 5.7 | 8.6 | 22.8 | 7.7 | 10.1 | 24.0 |
| Poly | 2 | N | - | 3.7 | 5.3 | 10.8 | 6.4 | 9.2 | 26.1 | 7.7 | 10.7 | 26.9 |
| Poly | 3 | N | - | 4.6 | 5.7 | 13.3 | 5.1 | 10.1 | 29.0 | 6.9 | 11.6 | 29.1 |
| Poly | 1 | Y | - | 3.1 | 5.2 | 10.6 | 5.7 | 8.6 | 22.8 | 7.7 | 10.1 | 24.0 |
| Poly | 2 | Y | - | 3.7 | 5.2 | 10.7 | 6.3 | 9.2 | 26.1 | 7.6 | 10.6 | 26.9 |
| Poly | 3 | Y | - | 4.3 | 5.6 | 13.2 | 5.3 | 10.1 | 29.0 | 6.9 | 11.6 | 29.1 |
| Interp | 1 | N | 32 | 8.0 | 19.9 | 61.8 | 8.1 | 14.3 | 35.4 | 15.5 | 24.5 | 70.3 |
| Interp | 2 | N | 32 | 11.7 | 21.0 | 58.8 | 9.2 | 15.3 | 42.5 | 17.1 | 25.9 | 67.5 |
| Interp | 3 | N | 32 | Did not converge | | | | | | | | |
| Interp | 1 | Y | 32 | 3.3 | 4.8 | 12.8 | 4.5 | 8.5 | 30.0 | 5.9 | 9.8 | 30.7 |
| Interp | 2 | Y | 32 | 2.5 | 4.8 | 13.0 | 5.1 | 9.6 | 28.1 | 6.0 | 10.8 | 28.3 |
| Interp | 3 | Y | 32 | 5.2 | 12.3 | 36.7 | 5.9 | 14.0 | 39.4 | 10.2 | 18.7 | 40.5 |
| Interp | 1 | N | 64 | 8.1 | 11.1 | 27.5 | 9.3 | 13.4 | 32.2 | 13.4 | 17.4 | 37.6 |
| Interp | 2 | N | 64 | 11.1 | 11.9 | 24.8 | 10.5 | 13.9 | 34.4 | 15.5 | 18.3 | 39.2 |
| Interp | 3 | N | 64 | 12.8 | 20.7 | 56.5 | 15.4 | 23.5 | 51.8 | 24.0 | 31.3 | 58.6 |
| Interp | 1 | Y | 64 | 3.0 | 4.7 | 10.8 | 3.6 | 7.3 | 21.7 | 5.2 | 8.7 | 22.5 |
| Interp | 2 | Y | 64 | 3.2 | 4.7 | 10.8 | 3.4 | 8.2 | 21.7 | 4.8 | 9.4 | 24.1 |
| Interp | 3 | Y | 64 | 3.6 | 6.7 | 19.7 | 5.8 | 15.5 | 56.2 | 8.1 | 16.9 | 56.6 |

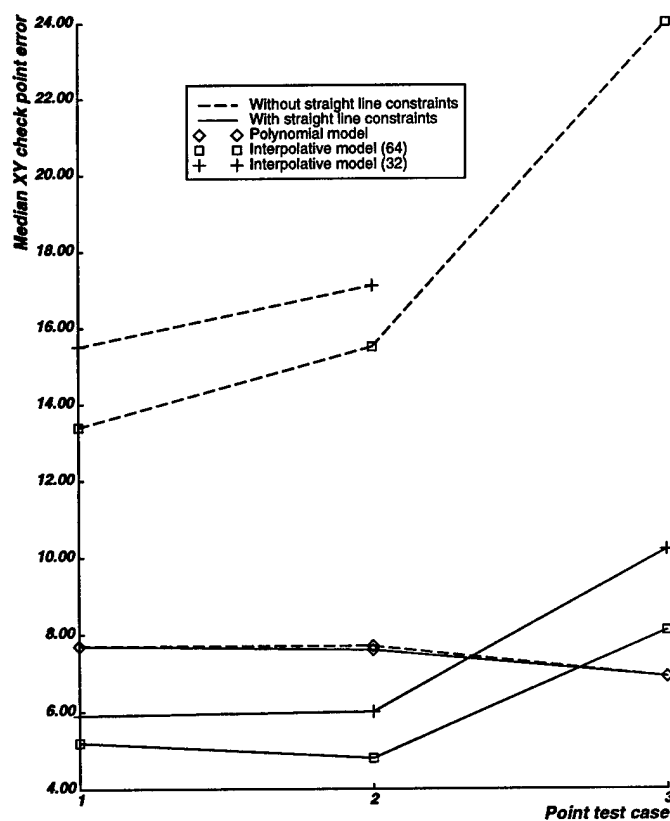
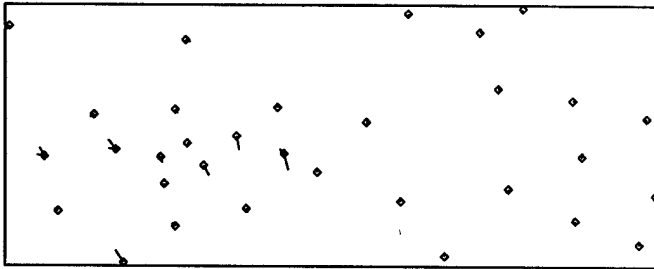


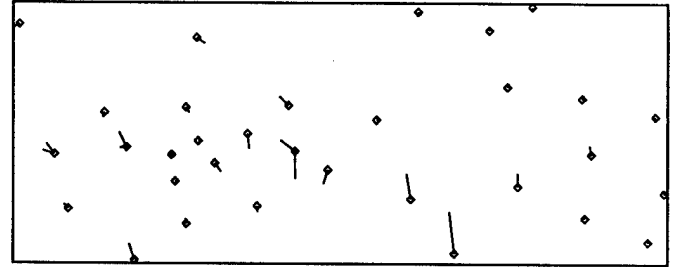
Figure 3: Median absolute XY check-point error, meters.

Table 3: Check-point error (meters) on each HYDICE image, using interpolative model.

| Image | Pt case | Lines | Ref. line spacing | X | | | Y | | | XY | | |
|-------|---------|-------|-------------------|-----|-----|------|-----|------|------|-----|------|------|
| | | | | Med | RMS | Max | Med | RMS | Max | Med | RMS | Max |
| 4_3 | 1 | Y | 64 | 4.1 | 4.9 | 9.7 | 3.4 | 3.6 | 5.9 | 6.0 | 6.1 | 9.8 |
| 5_3 | 1 | Y | 64 | 2.4 | 4.6 | 10.8 | 3.9 | 9.2 | 21.7 | 5.2 | 10.3 | 22.5 |
| 4_3 | 2 | Y | 64 | 3.9 | 4.8 | 9.6 | 3.5 | 4.6 | 10.9 | 5.6 | 6.6 | 12.5 |
| 5_3 | 2 | Y | 64 | 2.7 | 4.6 | 10.8 | 3.4 | 10.1 | 21.7 | 4.7 | 11.1 | 24.1 |
| 4_3 | 3 | Y | 64 | 3.7 | 8.4 | 19.7 | 4.8 | 7.0 | 14.7 | 8.2 | 10.9 | 24.6 |
| 5_3 | 3 | Y | 64 | 3.0 | 5.1 | 10.8 | 7.6 | 19.6 | 56.2 | 8.1 | 20.3 | 56.6 |



(a) Heavy point density (case 1).



(b) Sparse point density (case 3).

Figure 4: Check point errors for interpolative model with line constraints.

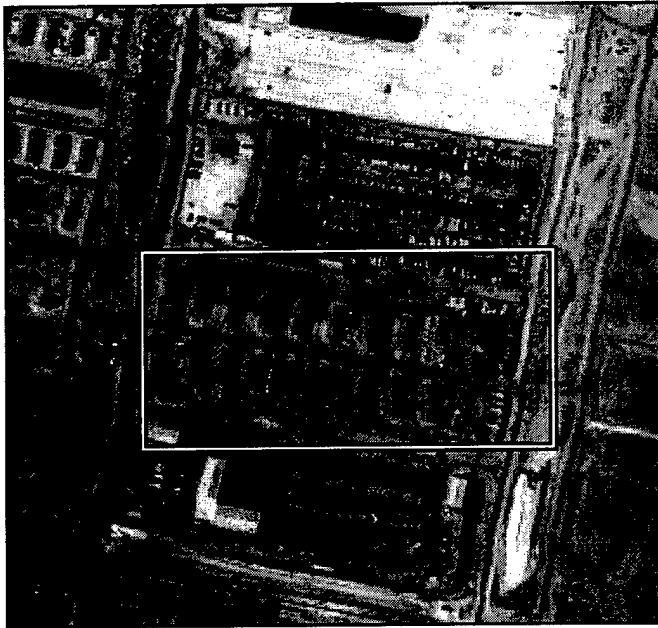
For this data set, the polynomial model generally performed better than the interpolative model without lines, but not as well as the interpolative model with straight line constraints. The interpolative model without straight line constraints degrades more rapidly than the polynomial model as the amount of control is decreased (going from the heavy (1) to the sparse (3) point densities). This is particularly evident in the maximum error statistic in the Y direction.

In nearly all cases, the error in the Y direction (approximately cross-strip) is worse than in the X direction (approximately along-strip). A possible explanation for this is uncompensated sensor roll, due to a combination of atmospheric turbulence and a malfunctioning stabilization platform.

Effectiveness of straight line constraints. The inclusion of straight line constraints in the interpolative model solutions improved the results in every case. While decreasing the number of tie points still increased check-point error, the results from the runs with sparse points (case 3) are still better than the results for the heavy point density (case 1) without lines. This indicates that straight line constraints can be used both to improve a solution or as an effective substitute for additional tie points; however, adding the straight line constraints to the polynomial model solution made only negligible differences. It may be that the polynomial model, with its more limited flexibility, is unable to use the additional information from the line constraints.

It is interesting to note the improvement in the X direction from the addition of the lines. The lines are selected parallel to the flight direction and would be expected to mostly improve positioning in the Y (cross-strip) direction. It is possible that since the lines make an approximate 30-degree angle to the flight direction, they add some geometric strength in the X direction.

Reference line spacing Decreasing the reference line spacing for the interpolative model will make the model more flexible by increasing its degrees of freedom. Given enough information to determine the model, it should recreate the platform motion more accurately and give better results. In this case, however, decreasing the reference line spacing generally degraded the results. The additional degrees of



(a) RADT9 test area from Flightline 4



(b) CHAFFEE test area from Flightline 7

Figure 5: Simulated Daedalus ATM near infrared imagery (Band 7) of classification test areas.

freedom were not adequately determined by the available information, and, in fact, the solution using the sparse point density without lines did not converge.

Variation between images. As mentioned above, the characteristics of the platform motion can change drastically during a mission. The two HYDICE images used in this experiment demonstrate this; examination of Figures 1(a) and 1(b) show that image 5.3 is much more deformed than image 4.3. Statistical evidence of this is given in Table 3 for a few selected test cases (interpolative model with line constraints). Note that the median deviations for the two images are very comparable for each case, but the maximum check-point deviations are much larger for image 5.3 than for 4.3.

Figure 4 shows the check-point errors for the heavy (1) and sparse (3) point densities (interpolative model using line constraints, 64 reference line spacing). Note that check-points that appear on both HYDICE images have two error vectors, since they are treated as independent points in each image. The sparse case shows much larger check-point errors for a few points; the largest for the sparse case is 56.6 meters, but 21.7 meters for the heavy case. In both cases, most points have relatively small errors, with the larger errors occurring in groups. These groupings tend to indicate areas of higher image deformation or weaknesses in the control configuration.

3. Automated Analysis of HYDICE imagery

Because of the volume of image data collected by the HYDICE hyperspectral sensor, these classification experiments used a reduced image dataset. To build on our previous experience with Daedalus ATM imagery, we simulated Daedalus ATM imagery by averaging the HYDICE imagery bands contained within the solar reflective bandpasses of the Daedalus ATM scanner (Table 4).

Figure 5 shows the two test areas used in the surface material classification experiments. The test areas' scene composition include motor pool/barracks (Figure 5(a)) and residential (Figure 5(b)) landscapes. Differing percentages and types of natural and man-made materials are present in each of these test areas.

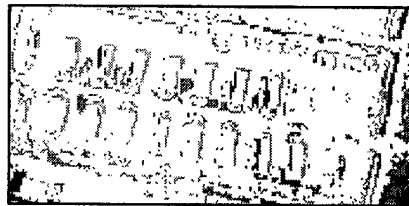
The test areas are from Flightlines 4 and 7, which have acquisition time differences of 60 minutes. Downwelling radiometric conditions between these flightlines changed significantly, as recorded by ground spec-

Table 4: Daedalus ATM spectral bandpasses.

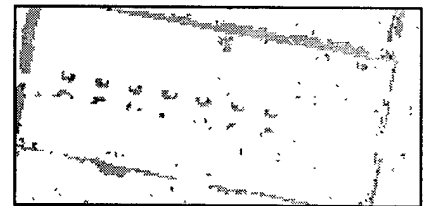
| Band Number | Bandpass (micrometer) | Band Number | Bandpass (micrometer) |
|-------------|-----------------------|-------------|-----------------------|
| 1 | 0.420 – 0.450 | 6 | 0.690 – 0.750 |
| 2 | 0.450 – 0.520 | 7 | 0.760 – 0.900 |
| 3 | 0.520 – 0.600 | 8 | 0.910 – 1.050 |
| 4 | 0.600 – 0.620 | 9 | 1.550 – 1.750 |
| 5 | 0.630 – 0.690 | 10 | 2.080 – 2.350 |



(a) RADT9 man-made surface/roofing



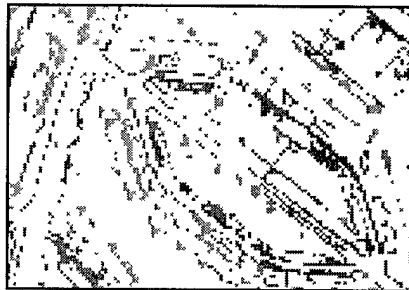
(b) RADT9 bare earth/shadow



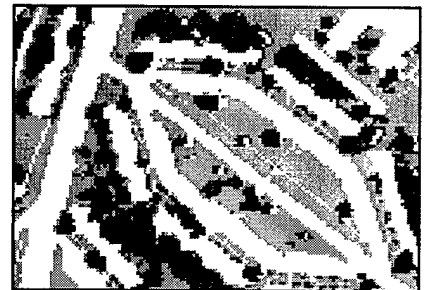
(c) RADT9 vegetation/water



(d) CHAFFEE man-made surface/roofing



(e) CHAFFEE bare earth/shadow



(f) CHAFFEE vegetation/water

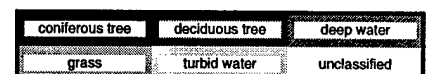
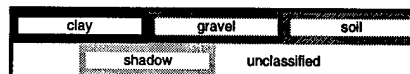
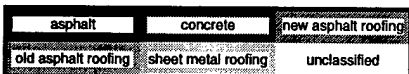


Figure 6: Test area subsection surface material classification.

tral radiance measurements during the overflights. To minimize the effects of changing solar illumination and atmospheric conditions between flightlines, the simulated Daedalus ATM imagery was converted to apparent reflectance by using the gray-scale panel imagery and spectral reflectance measurements to calculate band gain and offset coefficients for each flightline.

Manually-selected training sets for the materials listed in the "Fine Surface Material" column of Table 5 were compiled from an earlier section of Flightline 4. A Gaussian Maximum Likelihood (GML) classification was performed using the 10 simulated Daedalus ATM bands and selected training sets. Figure 6 shows a surface material subsection map from the resulting classification. These subsection maps correspond to the outlined regions shown in Figure 5 for the respective test areas.

The resulting surface material maps were evaluated against manually-generated surface material ground truths for each test area. Classification accuracies are 57.9 percent for RADT9 and 60.4 percent for CHAFFEE. From Table 6, almost 20 percent of RADT9's classification error is associated with confusion among concrete, asphalt, soil and gravel. Looking at Figure 6(a), there is breakup of the parking lot into asphalt and concrete sections probably influenced by surface weathering and vehicular traffic. Also, the barrack roofs fluctuate in surface material classification due to illumination changes influenced by building roof struc-

Table 5: Fine-to-coarse class grouping.

| Coarse Surface Material | Fine Surface Material |
|----------------------------|---|
| man-made surface | asphalt concrete |
| bare earth | soil clay gravel |
| vegetation | grass deciduous tree coniferous tree |
| water | deep water turbid water |
| man-made roofing | new asphalt roofing old asphalt roofing sheet metal roofing |
| shadow | shadow |

Table 6: RADT9 top 5 confusion pairs.

| Ground Truth Class | Classification Class | Number Confused | Error Percentage |
|-----------------------|-------------------------|--------------------|---------------------|
| concrete | asphalt | 7074 | 10.3% |
| soil | gravel | 2756 | 4.0% |
| grass | soil | 2233 | 3.3% |
| asphalt | soil | 1703 | 2.5% |
| concrete | soil | 1558 | 2.3% |
| Total | | 15324 | 22.4% |

Table 7: CHAFFEE top 5 confusion pairs.

| Ground Truth Class | Classification Class | Number Confused | Error Percentage |
|------------------------|-------------------------|--------------------|---------------------|
| shadow | deciduous tree | 3571 | 4.8% |
| deciduous tree | grass | 3447 | 4.7% |
| old asphalt roofing | concrete | 2522 | 3.4% |
| grass | deciduous tree | 2084 | 2.8% |
| asphalt | soil | 1647 | 2.2% |
| Total | | 13271 | 17.9% |

ture. Reviewing Table 7, approximately 12 percent of CHAFFEE's classification error belongs to shadow, deciduous tree and grass confusions. From Figure 5(b) and Figure 6(f), trees and grass dominate the scene content of this test area. Some of this reported error is inherent in the ground truth due to the complexity of attempting to segment out regions of overlapping tree shadows and canopies surrounded by grass.

We also are interested in coarse surface material classification, whereby the fine surface material classes are grouped into more general categories as listed in Table 5. This type of broad categorization is useful in identifying areas containing man-made or natural surface features. Table 8 and Table 9 display the

Table 8: RADT9 coarse classification error matrix.

| TEST | REFERENCE | | | | | | Row Total | Commission Error |
|--|------------------|------------|------------|-------|------------------|--------|-----------|------------------|
| | man-made surface | bare earth | vegetation | water | man-made roofing | shadow | | |
| man-made surface | 26677 | 1973 | 1509 | 0 | 1477 | 608 | 32244 | 17.3 |
| bare earth | 5129 | 7299 | 2444 | 0 | 254 | 58 | 15184 | 51.9 |
| vegetation | 377 | 822 | 14666 | 0 | 117 | 149 | 16131 | 9.1 |
| water | 0 | 0 | 0 | 0 | 0 | 0 | 0 | * |
| man-made roofing | 671 | 182 | 285 | 0 | 1598 | 367 | 3103 | 48.5 |
| shadow | 130 | 33 | 425 | 0 | 79 | 1153 | 1820 | 36.6 |
| Column Total | 32984 | 10309 | 19329 | 0 | 3525 | 2335 | 68482 | |
| Omission Error | 17.3 | 51.9 | 9.1 | * | 48.5 | 36.6 | | Percent |
| Overall Accuracy = 51393 / 68482 = 75.0% | | | | | | | | |

Table 9: CHAFFEE coarse classification error matrix.

| TEST | REFERENCE | | | | | | Row Total | Commission Error |
|--|------------------|------------|------------|-------|------------------|--------|-----------|------------------|
| | man-made surface | bare earth | vegetation | water | man-made roofing | shadow | | |
| man-made surface | 6693 | 0 | 1773 | 0 | 3809 | 921 | 13196 | 49.3 |
| bare earth | 2213 | 0 | 1891 | 0 | 684 | 548 | 5336 | 100.0 |
| vegetation | 472 | 0 | 43949 | 0 | 644 | 5986 | 51051 | 13.9 |
| water | 0 | 0 | 0 | 0 | 0 | 0 | 0 | * |
| man-made roofing | 80 | 0 | 92 | 0 | 564 | 116 | 852 | 33.8 |
| shadow | 77 | 0 | 496 | 0 | 318 | 2527 | 3418 | 26.1 |
| Column Total | 9535 | 0 | 48201 | 0 | 6019 | 10098 | 73853 | |
| Omission Error | 49.3 | * | 13.9 | * | 33.8 | 26.1 | | Percent |
| Overall Accuracy = 53733 / 73853 = 72.8% | | | | | | | | |

error matrices for the coarse classification for each of the test areas. Coarse classification accuracies range from 72.8 percent (CHAFFEE) to 75.0 percent (RADT9). For RADT9, the majority of the error (10.4 percent) involves man-made surface and bare earth confusions while CHAFFEE's dominant error (8.1 percent) is confusion between shadow and vegetation. These coarse surface material confusions have similar trends that were seen in the earlier fine material classification.

We are currently working on the use of HYDICE's high spectral resolution for spectral similarity and linear mixture analysis with ground-measured surface material reflectance curves.

4. Conclusions

This work has shown the effectiveness of straight-line constraints in the block adjustment of linear push-broom imagery when used in conjunction with an interpolative platform model. The techniques demonstrated can be used in the absence of navigation data, as was the case for the HYDICE imagery, or in conjunction with navigation data in order to improve the accuracy and reliability of the positioning solution. This work will be applied to the adjustment of our full block of HYDICE imagery, now in progress.

Despite the lack of navigation information in the current investigation, there is no theoretical or practical reason not to use these techniques in conjunction with GPS/INS data; indeed, our initial plan was to include navigation information in the block adjustment solution. Unless the navigation sensor accuracy and the system calibration are of very high order, or unless a very large number of high quality (possibly automatically generated) tie points are available, it would appear that the use of straight line constraints can make significant contributions to the accuracy of a block adjustment.

Our ongoing research will attempt to establish whether additional improvements in accuracy can be obtained or whether we are at the accuracy limits of the sensor/platform combination without the addition of further information. Possible avenues of investigation will include increasing the number of tie points by using automated measurement techniques [Heipke *et al.*, 1996] and experimentation with other types of geometric constraints, such as right angles.

With the acquisition of a high spatial resolution HYDICE image set, an opportunity exists to exploit the spectral information from hyperspectral imagery to aid urban scene analysis for cartographic feature extraction. Radiometric effects from changing solar illumination and atmospheric conditions must be accounted for in order to support comparison of surface material properties across HYDICE flightlines. To use the surface material information to its full potential, accurate geopositioning of HYDICE imagery is crucial for fusing surface material information with stereo and monocular cues.

References

- [Ford and McKeown, 1992a] Ford S.J. and D.M. McKeown, Jr. Utilization of multispectral imagery for cartographic feature extraction. In *Proceedings of the DARPA Image Understanding Workshop*, pp. 805-820, San Diego, CA, January 1992. Defense Advanced Research Projects Agency, Morgan Kaufmann Publishers, Inc.
- [Ford and McKeown, 1992b] Ford Stephen J. and David M. McKeown, Jr. Information fusion of multispectral imagery for cartographic feature extraction. In *International Archives of Photogrammetry and Remote Sensing: Interpretation of Photographic and Remote Sensing Data*, volume XVII, B7, Washington, D.C., 2-14 August 1992. XVIIth Congress, Commission VII.
- [Ford et al., 1997a] Ford Stephen J., Dirk Kalp, J. Chris McGlone, and David M. McKeown, Jr. Preliminary results on the analysis of HYDICE data for information fusion in cartographic feature extraction. In *Proceedings of the SPIE: Integrating Photogrammetric Techniques with Scene Analysis and Machine Vision III*, volume 3072, pp. 67-86, April 1997. Also available as Technical Report CMU-CS-97-116, School of Computer Science, Carnegie Mellon University, Pittsburgh, PA.
- [Ford et al., 1997b] Ford Stephen J., Dirk Kalp, J. Chris McGlone, and David M. McKeown, Jr. Preliminary results on the analysis of HYDICE data for information fusion in cartographic feature extraction. Technical Report CMU-CS-97-116, School of Computer Science, Carnegie Mellon University, Pittsburgh, PA, March 1997.
- [Ford et al., 1998] Ford Stephen J., J. Chris McGlone, Steven D. Cochran, Jefferey A. Shufelt, Wilson A. Harvey, and David M. McKeown, Jr. Analysis of HYDICE data for information fusion in cartographic feature extraction. In *Proceedings of the International Geoscience and Remote Sensing Symposium*, volume 5, pp. 2702-2706, Seattle, WA, 6-10 July 1998.
- [Heipke et al., 1996] Heipke C., W. Kornus, and A. Pfannenstein. The evaluation of MEOSS airborne three-line scanner imagery: Processing chain and results. *Photogrammetric Engineering and Remote Sensing*, 62(3):293-299, March 1996.
- [Kappus et al., 1996] Kappus Mary, William Aldrich, Ronald G. Resmini, and Peter Mitchell. The flexible HYDICE sensor's first year of operation. In *Proceedings of the Eleventh Thematic Conference and Workshops on Applied Geologic Remote Sensing*, volume 1, pp. 433-441, February 1996.
- [Kratky, 1989] Kratky V. Rigorous photogrammetric processing of SPOT images at CCM Canada. *Photogrammetria, Journal of the International Society for Photogrammetry and Remote Sensing*, 44:53-71, 1989.
- [McGlone and Mikhail, 1981] McGlone J.C. and E.M. Mikhail. Photogrammetric Analysis of Aircraft Multispectral Scanner Data. Technical Report CE-PH-81-3, School of Civil Engineering, Purdue University, West Lafayette, IN, October 1981.
- [McGlone and Mikhail, 1982] McGlone Chris and Edward M. Mikhail. Geometric constraints in multispectral scanner data. In *Proceedings of the 48th Annual Meeting, American Society of Photogrammetry*, pp. 563-572. American Society of Photogrammetry, March 1982.
- [McGlone and Mikhail, 1985] McGlone J.C. and E.M. Mikhail. Evaluation of Aircraft MSS Analytical Block Adjustment. *Photogrammetric Engineering and Remote Sensing*, 51(2):217-225, February 1985.
- [McGlone, 1995] McGlone Chris. Bundle adjustment with object space constraints for site modeling. In *Proceedings of the SPIE: Integrating Photogrammetric Techniques with Scene Analysis and Machine Vision*, volume 2486, pp. 25-36, April 1995.
- [McGlone, 1996] McGlone Chris. Sensor modeling in image registration. In *Digital Photogrammetry: An Addendum to the Manual of Photogrammetry*, pp. 115-123. American Society of Photogrammetry and Remote Sensing, 1996.
- [McGlone, 1998] McGlone C. Block adjustment of linear pushbroom imagery with geometric constraints. In *International Archives of Photogrammetry and Remote Sensing*, volume XXXII, B2, pp. 198-205, Cambridge, United Kingdom, 13-17 July 1998.

- [Mikhail, 1993] Mikhail Edward M. Linear features for photogrammetric restitution and object completion. In *Proceedings of the SPIE: Integrating Photogrammetric Techniques with Scene Analysis and Machine Vision*, volume 1944, pp. 16–30, September 1993.
- [Ohloff, 1995] Ohloff Timm. Block triangulation using three-line images. In D Fritsch and D Hobbie, Eds., *Photogrammetric Week 1995*, pp. 197–206. Wichmann, September 1995.
- [Paderes *et al.*, 1984] Paderes Fidel C., Edward M. Mikhail, and Wolfgang Förstner. Rectification of single and multiple frames of satellite scanner imagery using points and edges as control. In *NASA Symposium on Mathematical Pattern Recognition and Image Analysis*, 1984.
- [Press *et al.*, 1989] Press W.H., B.P. Flannery, S.A. Teukolsky, and W.T. Vetterling. *Numerical Recipes In C*. Cambridge University Press, Cambridge, MA, 1989.